

X-rays induced alterations in mechanical and biochemical properties of isolated SH-SY5Y nuclei

Laura Andolfi,¹ Roberta Meschini,² Silvia Filippi,² Diana E. Bedolla,^{3,4} Federica Piccirilli,³ Maria Lepore,⁵ Ines Delfino,^{2, *}

¹*Istituto Officina dei Materiali - CNR, Basovizza, I-34149 Trieste, Italy.*

²*Dipartimento di Scienze Ecologiche e Biologiche, Università degli Studi della Tuscia, I-01100 Viterbo, Italy.*

³*Elettra Sincrotrone Trieste, SISSI Beamline, I-34149 Basovizza, Trieste, Italy*

⁴*Area Science Park, I-34149 Padriciano, Trieste, Italy*

⁵*Dipartimento di Medicina Sperimentale, Università della Campania "L. Vanvitelli", I-80100 Napoli, Italy*

* *Corresponding author: delfino@unitus.it*

Abstract

Background

The use of ionizing radiations in radiotherapy is an effective and very common cancer treatment after surgery. Although ionizing-radiation DNA damages are extensively investigated, little is known about their effects on the other nuclear components, since their variations when studied in whole cells can be difficult to decouple from those of the cytoplasmatic structures. The organization of nuclear components plays a functional role since they are directly involved in some of the nuclear response to chemical or physical stimuli. For this reason, studying the X-ray effects on nuclear components is a crucial step in radiobiology.

Materials and methods

We have used Atomic Force Microscopy (AFM) and micro-FTIR to examine the biomechanical and biochemical properties of hydrated fixed nuclei isolated from neuroblastoma (SH-SY5Y) cells irradiated by 2, 4, 6 and 8 Gy X-ray doses.

Results

The experimental results have shown that, already at 2 Gy irradiation dose, the nuclei exhibit not only a DNA damage, but also relevant alterations of lipid saturation, protein secondary structure arrangement and a significant decrease in nuclear stiffness, which indicate a remarkable chromatin decondensation.

Conclusions and General significance

The present work demonstrates that a multi-technique approach, able to disclose multiple features, can be helpful to achieve a comprehensive picture of the X-ray irradiation effects of the nuclear components and distinguish them from those occurring at the level of cytoplasm.

Keywords: Isolated nuclei; nuclear mechanical properties; vibrational fingerprints; X-ray exposure; chromatin decondensation; FTIR and indentation-AFM investigation

Introduction

Radiotherapy is an effective cancer treatment after surgery, which can destroy cancer cells using ionizing radiation (photons, electrons, protons, and heavier particles, such as carbon ions), while trying to minimize damage to healthy tissues by generating energy deposition spurs directly damaging DNA as well as bursts of reactive oxygen species (ROS) mediating radiation effects at microscale level [1,2]. Ionizing radiation is thus both a formidable ally and a hazardous foe to human health. Given this two-fold nature of ionizing radiation, its use as cancer treatment method requires a continuous investigation about the interactions of radiation with cells and tissues to improve selectivity and specificity of the treatment.

The X-ray radiation induced injuries affect genome integrity and cell components [3,4]. As main direct effects, it induces DNA breaks, as single and double strand breaks (SSBs and DSBs), while among secondary effects there are the generation of ROS that oxidize proteins and lipids, and induce several damages to DNA, too [2,5]. Collectively, all these changes lead to cell death and/or mitotic failure. Although all these features are extensively investigated, little is known about the X-ray radiation effects on the other nuclear components, since their modifications can be difficult to decouple from those of the cytoplasmatic structures when studied in whole cell.

The nucleus is the largest organelle in cells, which, beyond housing the genome and serving as the site of DNA and RNA synthesis, transcription, and processing, has a fundamental role in coordinating cellular architecture and function. Within the nucleoplasm, DNA is wrapped around histones, forming higher-order structures that occupy distinct locations, which can be categorized as either open and transcriptionally active euchromatin or tightly packed and inactive heterochromatin [6]. Inside the nucleus we can also find spherical bodies called nucleoli, where ribosomes are assembled. The nucleus is enclosed by the nuclear envelope, a dual lipid bilayer that is connected by nuclear pore complexes that mediate nuclear-cytoplasmic transport. The nuclear lamina is a dense protein network consisting of integral membrane proteins and type V nuclear intermediate filaments (i.e., lamins A, B, and C) that provide mechanical support to the inner nuclear membrane [6]. Some of these nuclear

components are known to be active elements of mechanotransduction process. The deformation of the nucleus itself is emerging as a critical mechanosensory system, suggesting that the nuclear stiffness is essential to modulate cellular responses to intracellular and extracellular mechanical stimulation [7]. In this sense, the investigation of the isolated nuclei after irradiation can aid distinguishing the alterations strictly related to nuclear structures.

To examine the biomechanical and biochemical alterations of isolated nuclei from neuroblastoma cancer cells we used Atomic Force Microscopy (AFM) and micro-Fourier Transform InfraRed (FTIR) spectroscopy. We analysed fixed hydrated nuclei isolated from neuroblastoma (SH-SY5Y) cells after X-ray irradiation with 2, 4, 6 and 8 Gy doses, which are of medical interest for radiotherapy and radiobiology. In fact, cancer treatment by ionizing radiation typically occurs by administering daily fractions of doses on the order of 2 Gy. The overall treatment may last several weeks with the total dose necessary for local tumor control ranging between 50 and 60 Gy.

For the biomechanical analysis, AFM offers unrivaled versatility and sensitivity in measuring mechanical properties of various bio-systems. The technique was extensively used to describe the mechanical features of cancer cells with different degree of aggressiveness [8-11], also when exposed to low-LET proton beam [12] or to X-ray radiation [13-15]. AFM was also applied to characterize the mechanical features of isolated nuclei or intact nuclei within cells [16-17]. For instance, it was shown that isolated nuclei of leukaemia cells exhibit relevant mechanical differences as compared to normal lymphocytes: isolated nuclei from high-risk leukaemia cells show higher viscosity than their counterparts from normal lymphocytes, while nuclei from relapsed-patient's cells presented higher density than those from normal lymphocytes or standard- and high-risk leukaemia cells [18]. Non-invasive label-free vibrational spectroscopy, including FTIR and Raman spectroscopy, exploits the interaction between light and molecules to probe their vibrational modes and to obtain a “chemical fingerprint” of a sample. These techniques contributed to shed light on the effect of ionizing radiations on cells, especially on biochemical changes occurring in cell components, also at the level of sub-cellular regions [19-25]. They have provided important information about the radiation-induced

apoptosis in human lymphocytes [26] and the temporal evolution of the apoptotic process induced by gamma rays [27]. Likewise, the effects of different radiation doses on human keratinocytes, at different times after irradiation, was described by IR spectroscopy [28]. Micro-FTIR was used to study the radiation damage of biological samples as a limiting factor when X-ray microscopy is performed [29,30]. Always by micro-FTIR, X-ray irradiation induced modifications of membranes fluidity and secondary structure of proteins in neuroblastoma cells were described [24]. Nano- and micro-IR spectroscopy were used to study glioblastoma cells exposed to proton irradiation [31]. The DNA damage induced in prostate cancer cells by proton beam exposure was outlined by FTIR, also at the level of sub-cellular regions [19]. However, beyond DNA alterations, many inherent features of the nucleus are hidden by biochemical alterations occurring at the level of cytoplasmatic structures when whole cells are investigated. For this reason, UV radiation induced damages in single melanocytes and isolated nuclei were analysed by SR-FTIR microspectroscopy and 3D confocal Raman imaging. The vibrational technique findings showed similar spectra profile for both isolated nuclei and living cells [32].

The analysis of injury induced by radiation exposure can benefit from a multitechnique approach in which different features of nuclei (or cells) are detected. Combining mechanical and spectroscopic measurements provides the advantage both to study radiation induced effects and to correlate the altered mechanical properties of nuclei damage of specific nuclear components (e.g., DNA/RNA, proteins, lipids), identified by the biochemical fingerprints detected by FTIR, or to their organization, without using any labeling procedure. Such an approach could be helpful to make a step forward in the understanding of processes occurring in cells after X-ray exposition.

The results demonstrate that the combination of nanoindentation measurements by atomic force microscopy (AFM) with FTIR spectroscopy enable the access to multiple information about alterations occurring in nuclear components upon irradiation. In particular, we observe that upon 2 Gy irradiation the isolated nuclei exhibit a considerable nuclear softening accompanied by DNA

damage and chromatin decondensation, with significant alterations of nuclear proteins secondary structures and nuclear membrane lipid saturation.

Materials and methods

Cell culture, X-ray irradiation and nuclei isolation

Cells of the SH-SY5Y line (American Type Culture Collection, Manassas, VA, USA), a human cell line subcloned from a bone marrow biopsy taken from a four-year-old female with neuroblastoma, were used in this study. This cell line is a thrice-cloned subline of the neuroblastoma cell line SK-N-SH which was established in 1970 from a metastatic bone tumor that is often used as in vitro models of neuronal function and differentiation.

Cells were grown at 37 °C and 5% CO₂ in Dulbecco's Modified Eagle Medium (DMEM) supplemented with 15% fetal bovine serum, 1% penicillin, 1% streptomycin, and 1% L-glutamine. DMEM medium, fetal bovine serum, penicillin, L-glutamine, polylysine and formaldehyde were purchase from Sigma-Aldrich (Milano, Italia).

For each sample 5 x10⁵ cells were seeded onto 90 mm petri dishes and grown for 48 h before treatment. X-ray irradiation was performed, on ice, using a Gilardoni MGL 200/8D machine operating at 250 kVp and 6 mA (dose rate 60 cGy/min). Cells were exposed to various doses of X-rays (2, 4, 6, 8 Gy) and then investigated together with unexposed cells (0 Gy; control sample).

Immediately after X-ray exposure, nuclei were extracted and washed in 5 mM Tris-HCl and 0.5% Triton X-100. Afterward a homogenization through 1 ml syringe and centrifugation at 15.000 rpm for 5 minutes at 4 °C were performed. Extracted nuclei were fixed in 3.7% paraformaldehyde (PFA) in PBS solution for 20 min, transferred in NaCl 0.9% solution and then stored at 4°C.

Nuclear staining and fluorescence microscopy

Control and irradiated samples were stained with DAPI solution. Fluorescence images were acquired by an inverted microscope (Axiovert 200, Carl Zeiss, Germany), a 40X objective and 100X objective

(Zeiss, Switzerland), using an Olympus XM10 camera and X-Cite fluorescence lamp illuminator (Excelitas Technologies, Massachusetts, USA).

Atomic Force Microscopy measurements

A drop of 0.5% NaCl containing isolated nuclei was placed on a petri dish and allowed to deposit for 2 minutes. Afterward the petri dish was slowly filled with 0.5% NaCl solution.

Force spectroscopy measurements were performed by using a NanoWizard II Atomic Force Microscope (JPK Instruments, Berlin, Germany) equipped with an inverted optical microscope (Axiovert 200, Carl Zeiss, Germany). Silicon AFM cantilevers (CSG10 NT-MDT with Au back side coating) of nominal spring constant 0.11 N/m were used as indenter. Before each measurement the spring constant of cantilever was calibrated on glass cover slip by using the thermal noise method [33].

Individual nuclei were identified by using the optical microscope, and the size of the nucleus was evaluated by performing force mapping on individual nuclei with a grid of 32 pixel \times 32 pixel or 16 pixel \times 16 pixel, speed of 5 $\mu\text{m}/\text{sec}$ and load of 0.5 nN. Afterward the cantilever was moved over the centre of the nucleus and pressed down to indent it. The motion of the z-piezo and the force were recorded. Several force-distance curves were acquired for each nucleus (approximately 10 curves) with a force load of 0.5-1 nN at a rate of 5 $\mu\text{m}/\text{sec}$ in z closed loop feed-back mode. Measurements were performed on N= 44 for control nuclei, N=38 for 2Gy, N= 43 for 4Gy, N=35 for 6Gy, and N=38 for 8Gy irradiated samples.

Evaluation of Young's modulus

The elastic properties of isolated nuclei were assessed by evaluating the Young's modulus. This value can be extracted by fitting the force-indentation curve with the Hertz-Sneddon model [34], which describes the relation between the applied force F and the indentation depth δ in a soft sample. Hence, the approaching force-distance curves were converted into force-indentation curves by subtracting

the cantilever bending from the signal height to calculate indentation. The resulting curves were fitted with the following relation:

$$F = \frac{E}{1 - \nu^2} \left[\frac{2 \tan \alpha}{\pi} \delta^2 \right]$$

where F is the applied force, E is the Young's modulus, α is the half cone angle of the AFM probe used as indenter, ν is the sample's Poisson ratio (assumed to be 0.5 for biological materials) [35] and δ is the indentation depth. Fitting was performed setting a maximum value of 500 nm for the indentation depth. Examples of the obtained fitting curves for control and all irradiation doses are shown in Fig. S1. Those fitting curves featuring a R^2 lower than 0.9 were not considered in the present analysis. The entire procedure was performed with the routine of the JPK Data Processing software.

FTIR spectrum acquisition

FTIR measurements were performed at the Chemical and Life Sciences branch of the Infrared Beamline SISSI (Synchrotron Infrared Source for Spectroscopic and Imaging), Elettra Sincrotrone Trieste, Trieste, Italy (Proposal N. 20195090). A Hyperion 3000 VIS-IR microscope coupled with a Vertex 70 V interferometer and equipped with a HgCdTe (MCT_A) detector was used (Bruker Optics, Ettlingen, Germany). A drop of solutions containing fixed nuclei were placed, without any further treatment, into a specific in-house device available at SISSI beamline. It comprises two CaF_2 optical windows (1 mm thick, 13-mm diameter). For each sample, various microareas ($50 \times 50 \mu\text{m}^2$) containing densely packed nuclei were selected by optical microscopy. On these areas, spectra were collected in transmission mode in the MIR region ($4000\text{--}800 \text{ cm}^{-1}$), averaging 256 scans (spectral resolution 4 cm^{-1} , zero-filling factor 2, scanner velocity 40 kHz). Before each sample acquisition, a background spectrum was acquired on a clean CaF_2 window, while a 0.9 % NaCl physiological solution spectrum was collected each 10 spectra: in both cases, the same parameters for cell acquisition were used.

For each sample at least 35 spectra from nuclei were acquired. Triplicate of each sample were considered. A total of 600 FTIR spectra from nucleus were processed.

Analysis of FTIR spectra

All the acquired spectra were corrected for the contribution of atmospheric carbon dioxide with the Atmospheric Compensation routine of OPUS 7.5 software (Bruker Optics GmbH, Ettlingen, Germany). Hence, the spectral contributions of the aqueous medium were subtracted by running an in-house built Matlab algorithm, based on the optimization of the baseline flatness in the 2500–1850 cm^{-1} range containing the water combination band [36,37].

All the resulting spectra were processed via Standard Normal Variate (SNV) normalization procedure consisting in subtracting each spectrum by its own mean and dividing it by its own standard deviation. After SNV, each spectrum has a mean of 0 and a standard deviation of 1. These pre-treated spectra were considered and used for further analysis.

The spectra were then fitted by using a superposition of pseudo-Voigt shaped vibrational modes. For each spectrum, the starting conditions of fitting parameters were manually defined by inspecting the spectrum and its second derivative. At this aim, second derivative spectra were calculated for all the spectra, using a Savitsky-Golay smoothing algorithm (13 smoothing points) and a 3rd order polynomial approximation. After the manual selection of the starting conditions, a best-fit routine based on the Levenberg-Marquardt nonlinear least-square method was used to determine the optimized intensity, position, and width of the peaks. After the completion of the deconvolution procedure, 600 sets (one for each analysed spectrum) of fitted parameters were obtained and considered for further analysis.

The Amide I band was further examined since changes in protein configuration can induce meaningful variations in its characteristics. To investigate protein secondary structure, pseudo-Voigt shaped components were used to deconvolve the Amide I band. After the completion of the

deconvolution procedure of the Amide I band, 600 sets (one for each analysed spectrum) of the fitted parameters were obtained and considered for further analysis.

The relative intensity of each absorption band with respect to the overall intensity of the Amide I band was proportional to the relative amount of the structure in infrared spectra.

Afterwards, to obtain information from the intensity of the observed bands, a ratiometric approach was employed [24,38,39]: the ratios between the intensity of selected bands were calculated and analysed for each obtained set of fitting parameters. This approach offers the possibility to obtain quantitative information on the relative contributes of single bands and to get rid of eventual intensity changes related to different experimental conditions (i.e., sample thickness).

Average spectra here reported were obtained for the single irradiation treatment (not irradiated, irradiated by using 2, 4, 6, and 8 Gy X-ray dose), by averaging all the spectra taken from samples (about 100 for each irradiation treatment) characterized by the same irradiation treatment.

Second derivative calculation, spectra averaging, fitting procedure and ratios calculations were performed by using Orange-Quasar v. 1.4 software [40].

Statistical analysis

To detect statistically significant differences between FTIR-derived data obtained for control and irradiated sample groups (0 Gy vs 2 Gy, 0 Gy vs 4 Gy, 0 Gy vs 6 Gy, 0 Gy vs 8 Gy doses) a t-Student test (pairwise comparison between datasets comprising almost 100 statistical units each) was used. The same approach was employed to compare FTIR-derived data obtained for samples treated with increasing irradiation doses (2 Gy vs 4 Gy, 4 Gy vs 6 Gy, 6 Gy vs 8 Gy). t-tests were performed by using Orange-Quasar v. 1.4 software [40].

The Young's modulus data distributions did not pass the D'Agostino Pearson normality test. As result, the statistical difference between the Young's modulus values of control group and each irradiated samples, and for increasing irradiation doses (i.e. 2Gy vs 4Gy, 4Gy vs 6Gy, 6Gy vs 8Gy),

was evaluated by the non-parametric Mann–Whitney test (two-tailed distribution) with GraphPad Prism 5.0.

Results and Discussion

Morphology of individual nuclei

Before proceeding with the mechanical and spectroscopic measurements, the integrity of the isolated nuclei was analysed by bright field (Fig. 1A) and fluorescence images (Fig. 1B and C) acquired with different magnifications. The nuclei of control (0 Gy) and irradiated samples (for all considered doses) show an ovoidal shape with a well definite contour. The size of the nuclei was evaluated by the AFM height images acquired in force mapping mode (Fig. 1D). This modality enabled us the estimation of the nuclei size, without performing AFM scanning, which could distort the nuclei simply deposited on the surface of the petri dish.

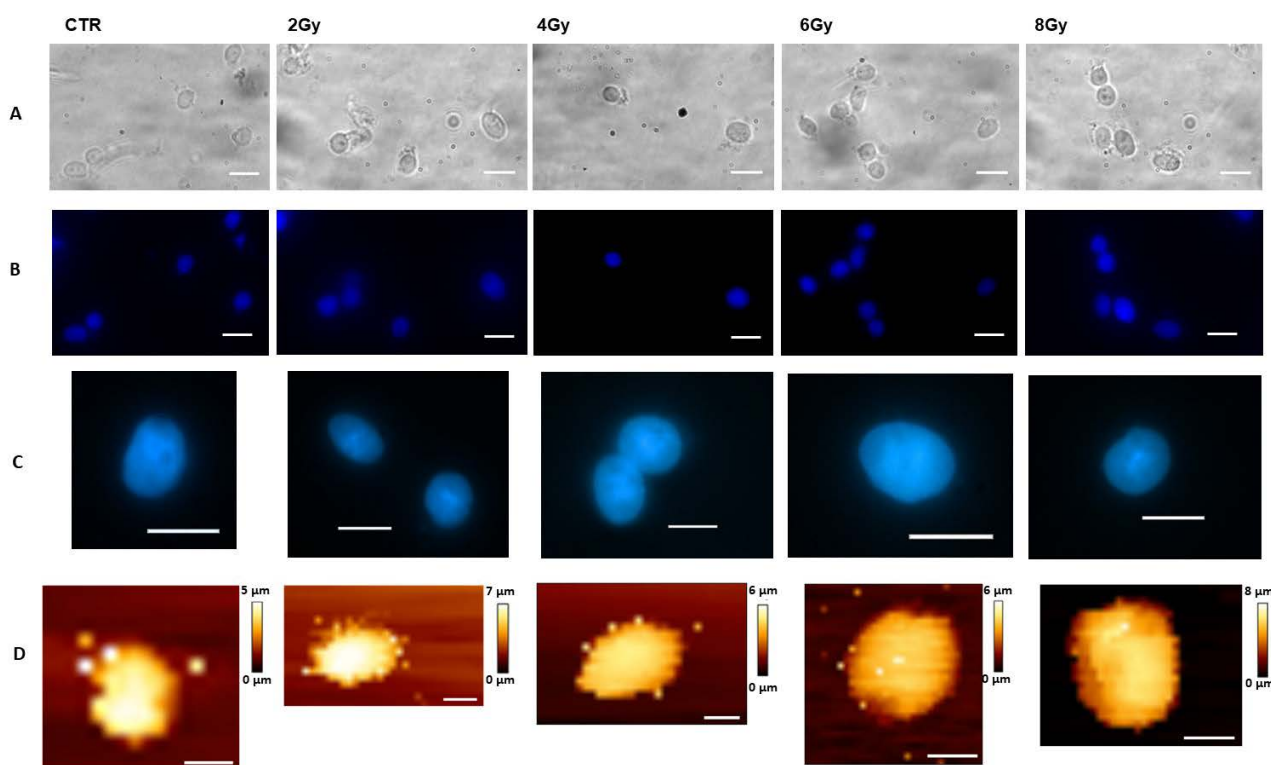


Figure 1. Morphology of isolated nuclei control (0 Gy) and irradiated (doses 2, 4, 6, 8 Gy): (A) bright field images (scale bar 5 μm); (B) epifluorescence microscopy images obtained with 40X objective (scale bar 5 μm); (C) higher resolution epifluorescence images obtained with 100X objective (scale bar 10 μm); (D) topography images as obtained by AFM force mapping (scale bar 5 μm).

We observed that for both control and irradiated samples the nuclei have height values from 4 to 7 μm . This height appears to be comparable with what reported in literature for nuclei inside the cell [6,16]. Of course, the nuclear shape and size within a cell depend on the cell type and can also vary with cell morphology, while for the isolated nuclei, which have no interactions with the cytoplasmatic organization, the nuclear size can be found even larger than that inside the cell [41]. These features, together with fluorescence images confirm the integrity of the extracted nuclei.

Mechanical properties of the nuclei

To evaluate the nucleus deformability isolated nuclei were selected, as shown in Fig. 2A, and indented by AFM tip. No displacement of the nuclei is observed under the indenting tip, as constantly monitored by bright field microscope. A representative example of force-indentation curves obtained is shown in Fig. 2B. The analysis of these curves according to the described fitting procedure provides the Young's modulus (E) values. A comparison of the evaluated E values for all irradiation doses samples and control samples is shown in Fig. 2C. The E values for the control samples (median value 2.2 kPa) are in general agreement with those observed in literature for isolated nuclei [42]. The comparison of the E values obtained for the control with those obtained for irradiated samples demonstrates a significant softening of the nuclei already at low irradiation dose (2 Gy) (1 kPa median value). Significant differences between increasing irradiation doses (2Gy vs 4Gy, 4Gy vs 6Gy, 6Gy vs 8Gy) were not observed. Accordingly, irradiation doses higher than 2Gy do not lead to a further decrement of the stiffness of the nuclei.

The stiffness values of isolated nuclei can vary as respect to the ones of the nucleus in living cells, where nucleus has numerous interactions with cytoskeleton and other cytoplasmatic organelles [41]. Moreover, it must be considered that the measured nuclei are in an artificial condition with respect to *in vivo* conditions. The PFA fixation modifies the membrane proteins and forms a matrix in which the membrane and lipids are trapped, and a natural clustering state is stabilized. In the case of cells,

this treatment is observed to induce hardening of cell surface as compared to live cells [43]. However, although the fixation process stiffens the cell surface, some experimental data demonstrate that the elasticity of fixed cells is still preserved up to 4% PFA [43, 44]. Likewise, we can expect that the elasticity of the nucleus can be preserved upon the fixation procedure here employed.

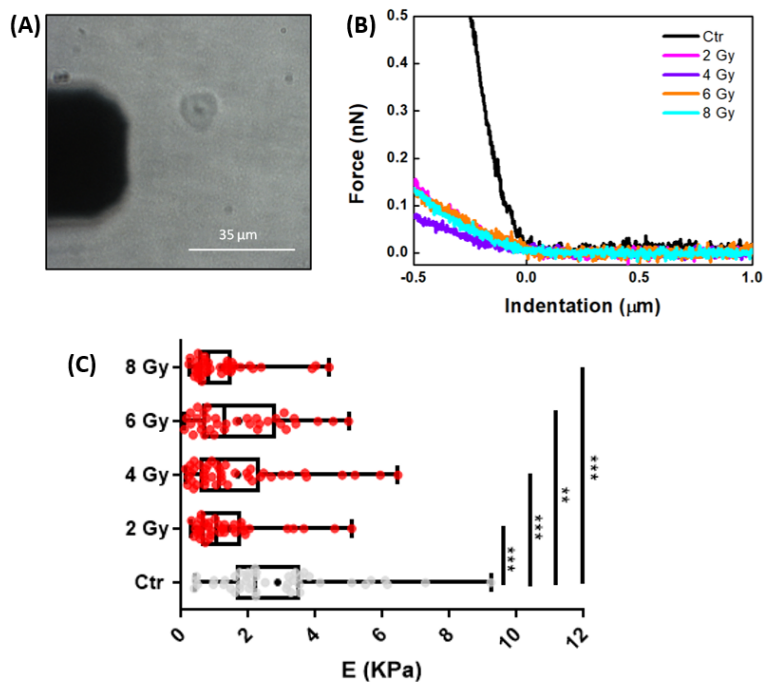


Figure 2. (A) Bright field image of isolated nuclei selected for indentation measurements; (B) example of the force-indentation curves obtained for control and at the different irradiation doses; (C) comparison of the E values obtained for the control (N= 44; 2Gy N=38, 4Gy N= 43, 6Gy N=35, and 8Gy N=38) are reported as box plot: the values inside the box represent the first (25%) and third quartile (75%), the (-) indicate the maximum and minimum values; the line within the box represents the median value (50%); while the mean value is indicated in the plot as (+). Significance is reported according to (**) $p < 0.01$, (***) $p < 0.001$.

In addition, in our case, the same procedure for extracting and fixing the isolated nuclei is used for both control and irradiated samples. Hence, it is reasonable to think that the fixed nuclei are still elastic and that the effects of extraction and fixation are the same for all the samples and that this factor equally contributes to the features of the control and the irradiated samples. As result the differences we observe are related to damage and alteration of nuclear organization determined by X-ray radiation.

Studies of nuclear deformations under applied stress have revealed that the overall mechanical behavior of the nucleus is determined by the nuclear lamina and the nuclear interior; the lipid nuclear membranes are considered to play only a minimal role in nuclear stiffness [45]. The alteration of nuclear organization and nuclear lamina interferes not only with the physical properties of the nucleus but also with its mechanotransduction mechanism [6]. As observed in some pathologies, for instance laminopathies, the mutation or content variation of lamin, a main constituent of the nuclear envelope, strongly affects the mechanical properties of the nuclei. The lamin A/C gene knockout in mouse embryonic fibroblasts lead to a loss of nuclear stiffness, along with a loss of the physical interactions between nuclear structures and the cytoskeleton. This determines a general cellular softening, which emphasizes the key role of lamins in maintaining cellular tensegrity [46]. Experiments with *Xenopus* oocytes highlight that the expression of lamin A affects nuclear stiffness, which increases in a concentration-dependent manner [47].

Within the nucleus, the DNA associates to histone cores to form nucleosomes, the building blocks of chromatin. A softening of nuclei is observed in correlation with chromatin decondensation [48]. Studies on isolated nuclei have shown that histone tail-tail interactions counter the outward entropic pressure of the DNA, and enzymatic disruption of these interactions can lead to chromatin decondensation and nuclear softening [49]. In addition, it has been shown that chromatin decondensation, due to trichostatin A treatment, induces a significant nuclear softening [50].

Hence, in line with the literature data reported and discussed above, the nuclear softening we observe suggests that the X-ray irradiation doses we have used can induce a relevant variation at the level of chromatin organization and/or nuclear lamina.

Spectroscopic features of the isolated nuclei

The spectra obtained by averaging the standard variate normalized FTIR spectra of the nuclei exposed to the different doses of X-rays are shown in Figure 3 separately for the high wavenumber region

(HWR: 3100 - 2800 cm^{-1} ; Fig. 3A), and for the low wavenumber region (LWR: 1750 - 950 cm^{-1} ; Fig. 3B).

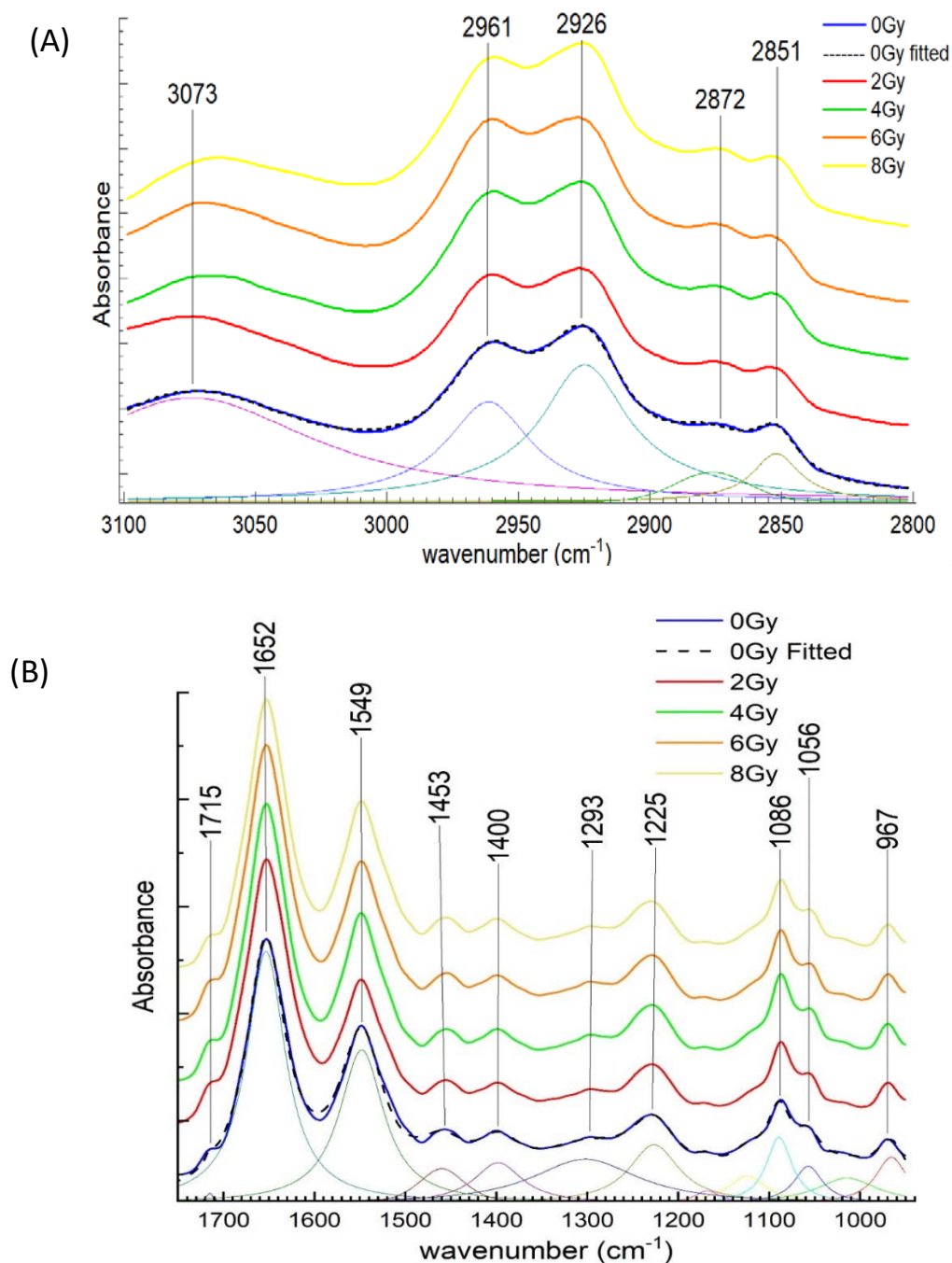


Figure 3. Average FTIR Absorbance spectra obtained for nuclei exposed to different irradiation doses. (A) High Wavenumber Range (HWR: 3100-2800 cm^{-1} region) and (B) Low Wavenumber Range (LWR: 1750-950 cm^{-1} region). 0Gy-fitted spectra are shown along with the single peaks contributing to the fitted curves. Main single peaks obtained by performing the deconvolution are labelled by indicating their positions.

To obtain information about the single peak characteristics, the deconvolution analysis was performed on the FTIR absorbance spectra, while the second derivative spectra (Fig. S2) was used to define the

starting conditions of the fitting procedure. Representative results of the deconvolution procedure for the 0Gy (control) spectra for both spectral regions are reported in Figure 3 where the single peaks contributing to signal and of overall fitted curves are shown. The positions of the most significant features are also reported in the same figure (they are referred to average spectrum of control samples).

The most relevant peaks are reported in Table 1 along with their assignments according to literature. Contributing bands related to the DNA and RNA (d), lipids and carbohydrates (l) and proteins (p) are observed as expected. In the HWR contributes mainly due to lipids are observed, while in the fingerprint region several DNA/RNA related bands are disclosed along with proteins-related Amide (I, II, III) bands and other proteins- and lipids-related signals. Most of the features was also found in the FTIR spectra of whole dehydrated fixed neuroblastoma cells [55], even if the relative intensities are different. This would be related to the role that the dehydration process can play in the contribution of the DNA in FTIR spectra at the cellular level, as widely discussed in ref. 57. Whereas some peaks mainly related to DNA/RNA are observed only when isolated nuclei are investigated. This is the case of the features at 1715 (d; base stacking mode, C=O stretching in purines and pyrimidines rings), 1293 (p; Amide III), 1172 (d; O–P–O stretching mode with a contribution from C–O–P stretching of protein and lipids), 1118 (d; skeletal structure around the C2 single bond and ribose), 1056 (d; PO_2^- ν_{sym} A form RNA) and 1019 cm^{-1} (d; furanose vibration).

Some of the peaks highlight changes in the position and/or intensity upon X-ray irradiation. To quantify these effects, the peak position and intensity were grouped according to the irradiation treatment and compared. The components featuring statistically significant changes with respect to control sample in position and/or intensity upon irradiation are listed in Table 2.

Relevant changes in positions are mainly observed for peaks related to proteins and DNA/RNA; shifts are also observed in the position of features related to lipids (l). The most significant position changes are observed for the peaks at 1605 (p; COO^- ν_{asym}) and 1086 cm^{-1} (d; O–P–O stretching mode), which show shift towards higher wavenumbers with respect to control at all doses while the peaks at around

3073 (assigned to $-\text{NH}_3$ asymmetric stretching of free amino acids) and 1056 cm^{-1} (present only in the nuclei FTIR spectra), which show a shift towards lower wavenumber for only the three highest doses.

Table 1. FT-IR peaks observed in the spectrum of control cells, with assignments in accordance with the data reported in the literature [26,28,51-56]; abbreviation: as = asymmetric, s = symmetric, v = stretching, δ = bending, sc = scissoring, vbr = vibration, a. a. = free amino acids. The indicated position of every peak is the position of the average peak positions obtained by averaging the values obtained by deconvolution of control (Ctrl-not irradiated)-nuclei spectra.

Peak position (cm^{-1})	DNA/RNA	Proteins	Lipids/Carbohydrates
3073		Amide B (-N-H v, δ)	
2961		CH ₃ as. v	CH ₃ as. v
2926			CH ₂ as. v
2872		CH ₃ s. v	CH ₃ s. v
2851			CH ₂ s. v
1715	base stacking mode: C=O stretching in purines and pyrimidines rings		
1617-1698	C=O, C=N, N-H of A, T, G, C	Amide I (C=O v, C-N v)	
1605		COO ⁻ as. v	
1549		Amide II (C-N v, C-NH δ)	
1517		Amide II	
1453		CH ₃ as. δ , CH ₂ sc.	CH ₃ as. δ , CH ₂ sc.
1422	ribose deformational vibration shoulders		COO ⁻ s. v polysaccharides
1400		COO ⁻ s. v	
1293		Amide III (-N-H δ , -C-N v) and δ (CH ₂) sensitive to secondary structure folding	
1225	$v_{\text{asym}}(\text{O-P-O})$ DNA backbone, sensitive to conformational changes	C-O-P v	
1172	Sugar -phosphate backbone vibration $v_{\text{asym}}(\text{O-P-O})$ A form RNA; Ribose		
1118	Stretching vibration of the skeletal structure around the C2 single bond; OH group of RNA and NTPs		
1086	$v_{\text{sym}}(\text{P-O-C})$ $v_{\text{sym}}(\text{O-P-O})$, DNA backbone,	C-O-P v	
1056	$v(\text{C-O})$ DNA backbone, $v_{\text{asym}}(\text{O-P-O})$ A form RNA		
1019	Furanose vibration		
967	C-O stretching; PO ₄ ⁻ s. v	C-O v, C=C v (a. a.)	

Among the other features observed only in FTIR spectra of isolated nuclei, the 1715-, 1172-, and 1118-cm⁻¹ bands experience a shift towards higher wavenumbers at two doses (6 and 8 Gy for the first two peaks). The box plot representations of the discussed positions and amplitudes are reported in Figures S3 and S4.

Table 2. Information on modifications of intensity and/or position peak occurring upon X-ray irradiation. Peaks featuring statistically significant changes of the mean obtained for irradiated samples (considered separately according to the dose) as compared with the corresponding one obtained for Ctrl (not irradiated) -related samples. Comparison between Ctrl-related mean and 2Gy-, 4Gy-, 6Gy and 8Gy-dose irradiate samples were performed by t-Student test with significance level=0.05. Positions and/or amplitude means featuring $p < 0.05$ upon comparison with mean obtained from 0Gy-related spectra are reported. Legend for changes: ↓ - decrease in intensity with respect to control, ↑ - increase in intensity with respect to control, ← - shift towards higher wavenumber as compared to control, → - shift towards lower wavenumber as compared to control. Legend for assignment: p - protein, l - lipids&carbohydrates, d - DNA/RNA.

0Gy Peak Position (cm ⁻¹)	2Gy	4Gy	6Gy	8Gy	Assignment
3081		→	→	→	P
2961	←↓				p,l
2926	←	↑	↑	↑	L
2872	↑	→	→↑	↑	p,l
2851				↑	L
1715	↓	↓	↓	←↓	D
1698	↑		↑		P
1661		↓	↓	↓	P
1647	↓		↓	↓	P
1635			→	→↑	P
1617	←				P
1605	←	←	←	←	P
1549	←	↑	→	→	P
1517	←				P
1453		→			L
1422		←			L
1293	↓	→↓	↓	↓	P
1225	↓	↓	↓	↓	d,p
1172	←	←↓	↓	↓	D
1118	←↓	↓	←↓	↓	D
1086	←	←↑	←	←	d,p
1056		→	→	→	D
1019	↓		↓	↓	D
967		↓		↓	d,p

The changes observed in position and intensity of the feature at 1715 cm⁻¹ agree with what found in studies about cells irradiated with various ionizing radiation (protons, UVC, X- and γ-rays). Such

evidence was associated with base-pair damage including purine, pyrimidine dimer formation and 6–4 lesions and local rupture of base-paired structures [56].

Regarding peak intensity variations, the most significant ones are observed for the features located at 1019 (d), 1118 (d), 1225 (d,p; ν_{asym} O–P–O DNA backbone and ν C–O–P), along with features located at 1635, 1647, 1661, and 1697 cm^{-1} that are all related to Amide I (p). The intensity of an infrared band is assumed to be proportional to the concentration of the species that are associated with the band [58–60]. However, the use of band absorbance values themselves for quantitative analysis can be dependent on experimental artefacts, such as variations in sample thickness. For this reason, specific intensity ratios, related to protein content, rearrangement, and phosphorylation, DNA content and modification, and lipid content and saturation, has been used [24,38,39]. All the ratios here considered are reported in Table 3.

Table 3. A_x/A_y indicate the ratio between the value of the intensity (as obtained by fitting procedure) of selected band [24 and references therein,38,39,53], located at x and y position, respectively). Abbreviation: as = asymmetric, s = symmetric, ν = stretching, δ = bending, sc = scissoring.

Ratio A_x/A_y	Biomolecular Origin	Indication
A_{1652}/A_{1549}	Amide I/Amide II	Protein rearrangement (PR)
A_{1086}/A_{2961}	PO_2^- s. ν , C–O–P ν /CH ₃ as. ν	Protein phosphorylation (PP)
A_{1652}/A_{1225}	Amide I/ PO_2^- as. ν	Protein/DNA content (PD1)
A_{1652}/A_{1086}	Amide I/ PO_2^- s. ν	Protein/DNA content (PD2)
A_{1400}/A_{2961}	COO– s. ν /CH ₃ as. ν	Protein/Lipid content (PL)
A_{2926}/A_{2961}	CH ₂ as. ν /CH ₃ as. ν	Lipid saturation (LS)
A_{1225}/A_{1086}	PO_2^- as. ν , C–O–P ν / PO_2^- s. ν , C–O–P ν	DNA modification (DM)
A_{1019}/A_{1086}	Furanose vib. / PO_2^- s. ν , C–O–P ν	DNA modification (D1)
A_{1056}/A_{1118}	DNA C–O ν , RNA PO_2^- as. ν /Ribose vib.	DNA modification (D2)
A_{1118}/A_{1225}	Ribose vib./ PO_2^- as. ν	DNA modification (D3)
A_{1056}/A_{1225}	DNA C–O ν , RNA PO_2^- as. ν / DNA PO_2^- as. ν	DNA modification (D4)
A_{1715}/A_{1086}	C=O ν / DNA PO_2^- s. ν	DNA modification (D5)
A_{1715}/A_{1225}	C=O ν / DNA PO_2^- as. ν	DNA modification (D6)
A_{1715}/A_{1019}	C=O ν / Furanose vib.	DNA modification (D7)

Figures 4 and 5 show the box plot representations of the ratio values obtained for control and irradiated samples along with information about the results of the pairwise comparison of single

irradiated groups with the corresponding control ones, showing that there are significant differences in various cases. Figure 4 shows the ratios involving only DNA-related features (DM and D1-D7), while in Figure 5 the results regarding protein-related (PR, PP, PD1, PD2, PL) and lipid-related (PL, LS) ratios are reported. At all radiation doses the DM ratio, related to DNA structure modifications, shows values significantly lower than the one observed for the control sample. This behaviour of DM vs dose is opposite to what observed when whole neuroblastoma cells were analysed by FTIR. This would be related to the effect of extra nucleus components, such as extra nucleus RNA and mitochondrial DNA. The same behaviour is observed for D7 ratio, i.e., D7 values obtained for irradiated samples are lower, for all the doses, than the corresponding value obtained for the control samples, suggesting that the relative intensity of the signal due to base stacking mode with respect to that of furanose ring vibration is lower in irradiated nuclei than in control ones. It is worth noting that this behaviour can be due to the decreased intensity of the 1715-cm^{-1} band, observed in Table 2, which is known to be a marker of DNA damage also in cells [56]. D1, D5 and D6 ratios have similar behaviour as a function of the dose: they all show a decrease with respect to control at all the doses, being statistically significant only at the highest doses (6, 8 Gy). This can indicate that, at these doses, the relative contribute of the furanose vibration decreases with respect to DNA O–P–O symmetric mode (D1) and that 1715-cm^{-1} mode (C=O base stacking mode) decreases with respect to DNA O–P–O symmetric and asymmetric mode (D5 and D6, respectively) and the relative contribute of decreases with respect to DNA O–P–O symmetric and asymmetric vibration (D6). D2 (giving information about the relative contribute of DNA C-O vibration with respect to that coming from ribose signal and RNA skeletal structure C2-OH group) and D4 (contribute of ribose signal and RNA skeletal structure C2-OH group with respect to contribute coming from to DNA O–P–O asymmetric and asymmetric vibration) ratios show a value significantly higher than the control one only at 4Gy. At the same dose D3 ratio shows the only value

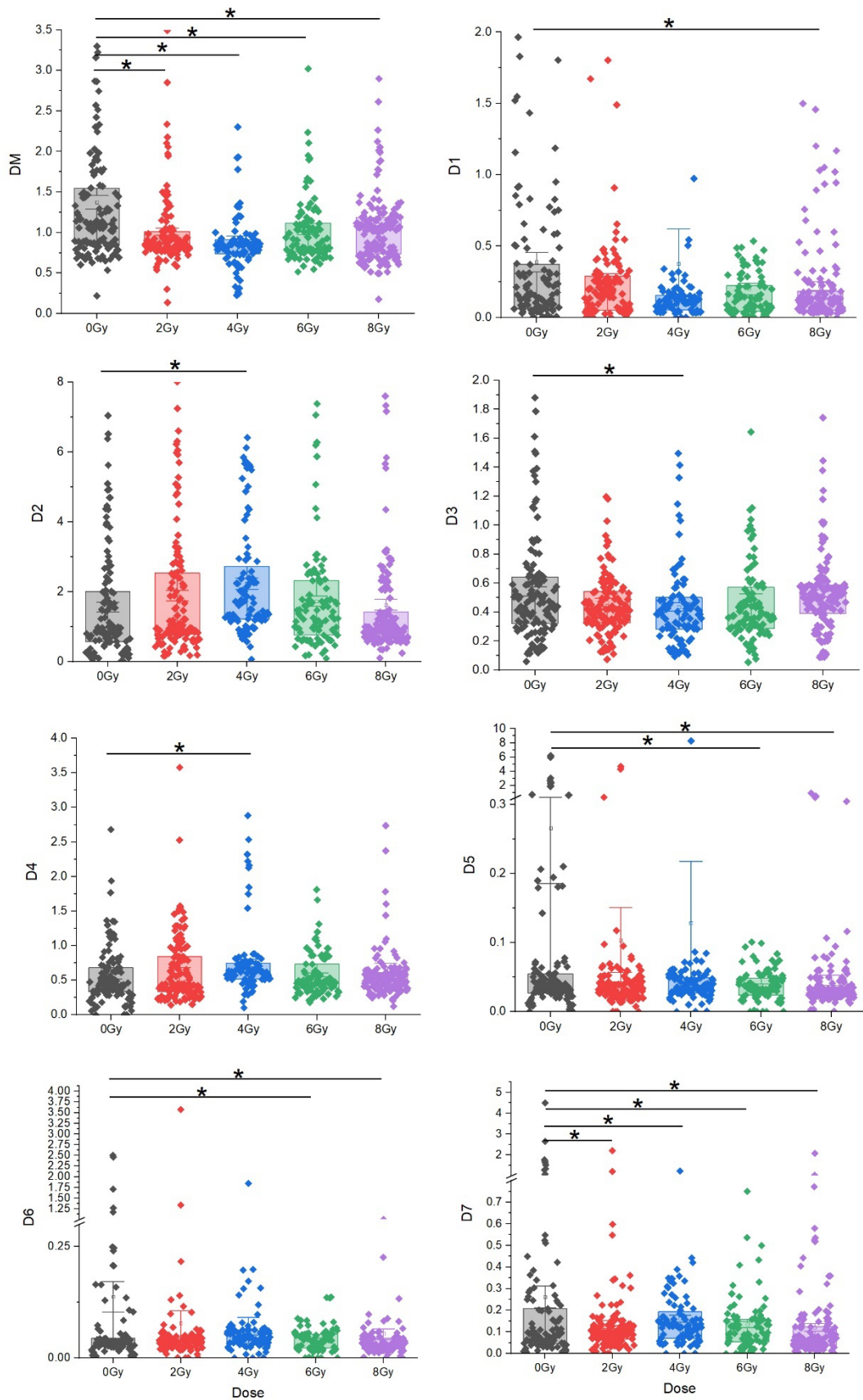


Figure 4. Box-plot representation (including standard errors) of the ratios reported in Table 3 involving DNA-related features; data are grouped according to the irradiation treatment, error bars representing the standard errors. The asterisks indicate the sub-datasets featuring a mean which is statistically significantly different from the corresponding control mean ($p \leq 0.05$).

which is significantly different from the control one: a contribution of ribose lower than the one coming from the RNA skeletal structure C2-OH group is observed.

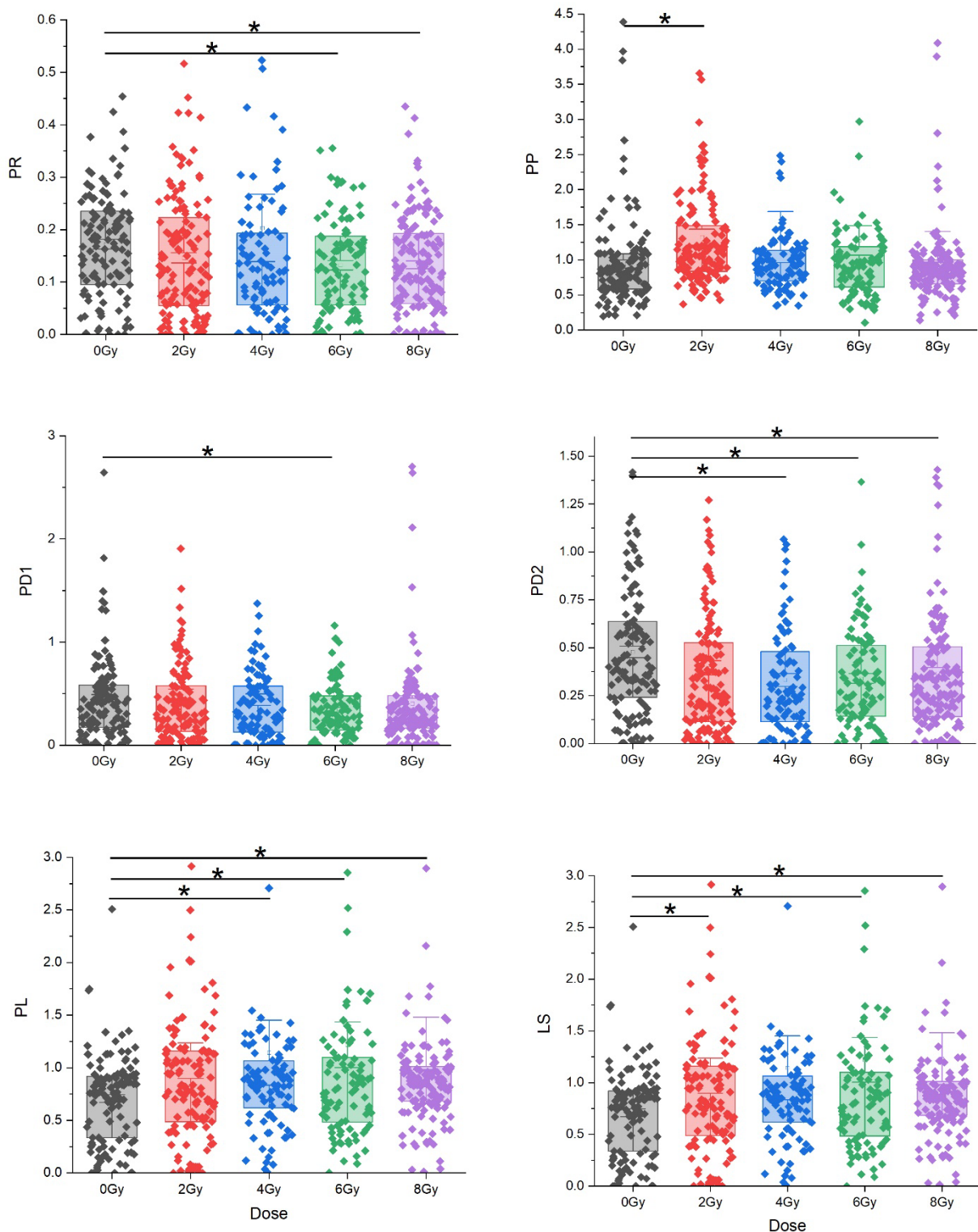


Figure 5. Box-plot representation (including standard errors) of the ratios indicated in Table 3 involving proteins- and lipids-related features; data are grouped according to the irradiation treatment; the error bars represent the standard errors. The asterisks indicate the sub-datasets featuring a mean which statistically significant different from the corresponding control mean ($p \leq 0.05$).

Since changes in the conformation and dynamics of the sugar moiety alter the local and potentially global structure and plasticity of nucleic acids [61], the discussed results can be related to such kinds of processes occurring upon irradiation with 4Gy X-ray.

PD1 and PD2 ratios show changes upon doses (Fig. 5): PD1 is significantly decreased at 6 Gy while PD2 is decreased at 4, 6 and 8 Gy. The overall panel of modifications evidenced by PD1, PD2, and DM agrees with the results obtained in other cell systems exposed to ionizing radiation and it is thought to indicate the occurrence of damage in the primary, secondary, and tertiary structure of nucleic acid [62].

Regarding the other evaluated ratios, protein phosphorylation ratio (PP) seems to be increased at all doses with respect to the value obtained for untreated (0 Gy) nuclei, even if the change is statistically significant only at 2 Gy. PL ratio, related to protein/lipid contribute, is higher than the control value at all the doses (changes are significant at the three highest doses). Similar results are obtained for the LS ratio, related to lipid saturation, which is higher than the value obtained for 0Gy-samples at all doses even if the difference is statistically significant only at 2, 6 and 8 Gy. The same results were observed for PL and LS ratio calculated from FTIR spectra of whole dehydrated SH-SY5Y cells [24]. In the case of cells, these findings were discussed in terms of possible cell apoptosis process that can occur together with several membrane changes, such as phosphatidylserine exposure, membrane blebbing, and vesicle formation. An increase of lipid saturation is thought to lead to membrane stiffening [63].

Opposite to the case of PL and LS ratios, when FTIR spectra of whole neuroblastoma cells were considered, PP ratio remained unchanged upon X-ray irradiation (same doses as those of the present study) [24]. This suggests that the phosphorylation-related processes involve nucleus-embedded proteins in a different way with respect to other proteins in cells. This result is of interest given the crucial role played by phosphorylation processes in DNA damage and in DNA response processes, as witnessed by studies focused on nuclear protein phosphorylation, that evidenced hyperphosphorylation of *Xenopus* homologue of 53BP1 (XL53BP1) after X-ray irradiation [64]. This

further confirms that the FTIR study of the isolated nuclei can shed some light also in the radiation-induced phosphorylation which is a crucial point in understanding radiation-induced damage and related DNA repairing processes.

PR ratio obtained for nuclei (Fig. 5), associated with protein rearrangement, has a lower value with respect to the 0Gy-value at 6 Gy- and 8 Gy-values, thus suggesting significant changes in nuclear protein secondary structure at the two highest irradiation doses.

To further examine protein rearrangement, the analysis of the different peaks constituting the Amide I band can offer precise information about the secondary structure of proteins and their conformational changes occurring upon irradiation at different ionizing radiation doses. In the present case, the Amide I band of control and irradiated samples was analysed using subcomponents related to parallel β -sheets, anti-parallel β -sheets, α -helix, and β -turn and unordered structures. An example of the deconvolution procedure for the Amide I is shown in Figure S5. The relative contributes, obtained as ratios of the intensity of the selected peaks and the overall Amide I signal, are shown in Figure 6.

The results confirm the occurrence of a protein rearrangement, which, in turn, does not seem to have a simple behaviour depending on the dose. The most significant effect is observed for β -sheets (a decreased contribution is seen at 2 and 4 Gy) and β -turn (increased contribution at 4, 6 and 8 Gy, although the change at 6 Gy is not statistically significant). Contribute due to α -helix is decreased at all doses with respect to control sample, significant difference having been observed only at 4 Gy. These results are in quite good agreement with those obtained for neuroblastoma cells [24]. In fact, PR (called PR1 in ref. 24) of irradiated cells is significantly lower than the control one at all the doses, thus suggesting a change in the relative contribution of the secondary structures, which is different from those observed for isolated nuclei.

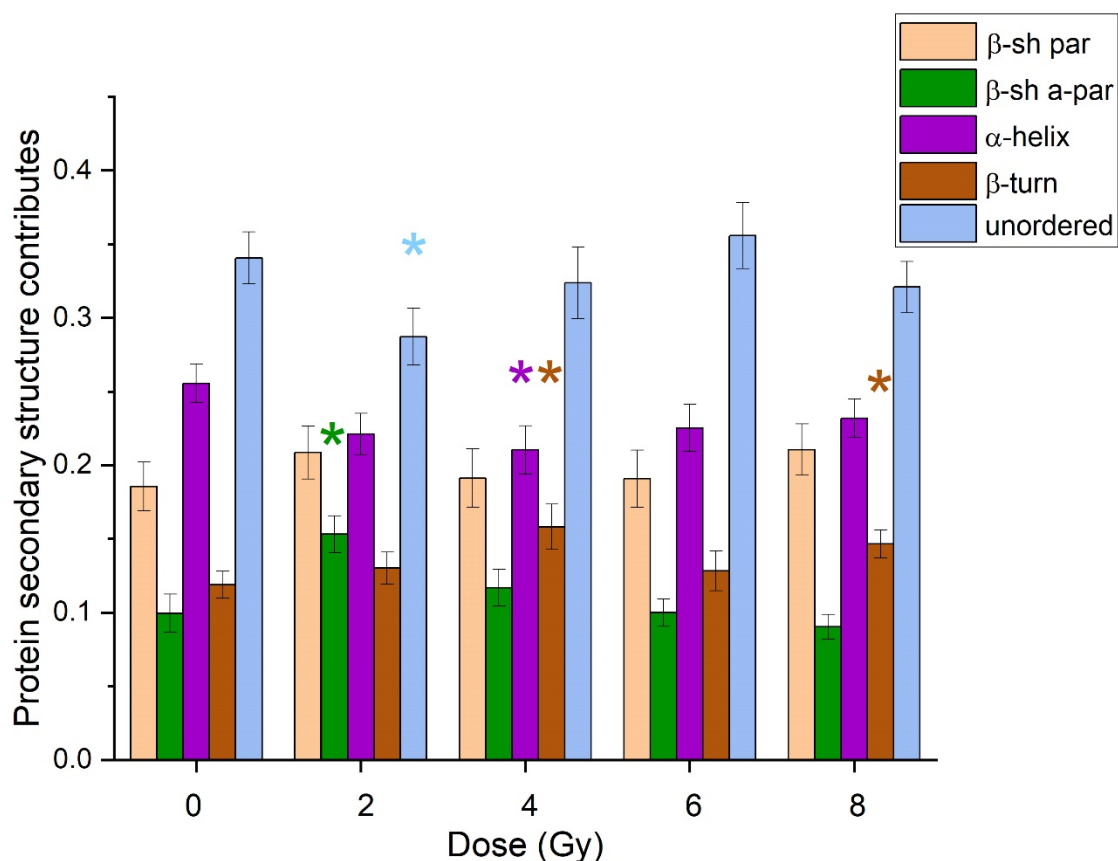


Figure 6. Bar-plot representation of secondary protein structure contributions to Amide I band ($1600\text{--}1700\text{ cm}^{-1}$) with dose; the error bars represent the standard errors; asterisks of different colours indicate a significant difference in respect to the corresponding control mean of the specific component ($p \leq 0.05$). Legend abbreviations: β -sh par: parallel β -sheet; β -sh a-par: anti-parallel β -sheet.

The complex behaviour in relative protein secondary structure contributions observed for nuclei agrees with literature reports showing that it is not possible to find a common behaviour of nuclear proteins in response to ionizing radiation. It is known, for instance, that histones undergo secondary structure changes upon X-ray irradiation, and that the specific changes can depend on the single histones. Upon 40Gy-X-ray irradiation, a change from in turn and β -strand to α -helix is observed in histone H2A-H2B induced by DNA damage response [66], while histone H3-H4 shows an increase in turn, β -strand and unordered structures and a decrease in α -helix contribution [67].

Interestingly, similar effects in DNA and protein related FTIR features were observed in *in situ* infrared spectroscopic study of spermatozoa by Oldenhof and coworkers [68]. In particular, it revealed that characteristic bands arising from the DNA backbone (modes at $1225, 1086, 1056\text{ cm}^{-1}$)

changed in response to induced oxidative damage and chromatin decondensation. Specifically, a decreased value of the asymmetric to symmetric phosphate band intensity (i.e., the here labelled DM ratio) was observed as chromatin condensation degree decreases, suggesting that this band ratio is sensitive to the degree of chromatin condensation. It is worth to note that changes in the amide-I region denoting concomitant changes in protein secondary structure were found. According to these findings, the decreased DM value observed for nuclei (opposite to DM values for whole neuroblastoma cells) suggests that chromatin decondensation, and changes related to nuclear protein structure, occurs upon X-ray irradiation at all doses.

Standard geno/cytotoxicity assays, such as Comet assay and micronuclei analysis of control and irradiated samples at all considered doses (2, 4, 6, 8 Gy), demonstrate a dose-dependent DNA damage, in agreement with data reported in literature [69, 70], continuously increasing as the irradiation dose increases (see Supplementary Materials).

The biochemical and mechanical characterisation of the nuclei highlights that, beside DNA damage, further alterations of other nuclear components can be revealed.

The stiffness of the nuclei does not follow the same dose-dependent trend of bioassays, but rather a significant softening already at 2 Gy, that does not decrease any further when increasing the irradiation dose up to 8 Gy. This trend suggests that notable alterations of nuclear components occur already at the lowest irradiation dose used. At the same irradiation dose, the spectroscopic analysis highlights the presence of remarkable variations in biochemical features, not only related to DNA damage but even to proteins and lipids. Indeed, DM, LS, and D7 ratios show a change at 2 Gy, thus behaving like the nuclear stiffness. For almost all discussed FTIR-derived ratios there is no statistically significant differences when pairwise comparison between data regarding increasing irradiation doses are considered (2Gy vs 4Gy, 4Gy vs 6Gy, 6Gy vs 8Gy). This confirms a significant modification of the nuclei already at 2Gy irradiation dose and suggests that minor changes, eventually due to increasing irradiation doses, cannot be detected in our spectra obtained on microareas containing densely packed nuclei. By using Comet assay, we evaluate the relative number of damaged

nuclei (Table S1). Interestingly, we observed that, already at 2Gy, 78% of nuclei appears to be damaged, while between 4Gy and 8Gy the number of damaged nuclei increases only of 20%. These data further confirm the results of mechanical and spectroscopical analysis, where a remarkable alteration of the nuclei at 2Gy irradiation dose is observed.

These results are consistent with previous studies, in which it was observed that chromatin decondensation and DNA damage are strictly associated with an increased nuclei deformability. The knock down of heterochromatin protein 1a (HP1a) highlighted that there is a significant decrease in the apparent Young's modulus of the MCF7-HP1a knock down cells as compared with control nuclei, reflecting the altered organization of the peripheral heterochromatin and changes to Lamin A/C dynamics observed in these nuclei [17]. Likewise, DNA damage induced by cisplatin treatment was observed to lead to a significant softening of nuclei [42].

Hence, our findings, in agreement with data reported in literature, demonstrate that an irradiation of 2Gy induces a considerable alteration of the nuclei that involves DNA damage along with a notable chromatin decondensation, and an increase in membrane lipid saturation.

Conclusions

We have demonstrated that the combination of AFM and FTIR measurements of hydrated fixed isolated nuclei can be very useful to detect relevant alterations associated with the nuclear organization. The comparison of these findings with that obtained on whole cells can help to disentangle X-ray irradiation effects related to nucleus from those related to cytoplasmatic structures. We have observed that upon irradiation with 2 Gy-X-rays the nuclei isolated from neuroblastoma cells exhibit a considerable nuclear softening accompanied by DNA damage, with significant alterations of nuclear proteins secondary structures and nuclear membrane lipid saturation. Increasing the irradiation dose up to 8Gy seems to not significantly change the overall effect.

The analysis of these features might be of relevance since, after irradiation, cells can recover and repair the DNA, but the recovery process could not involve lipid arrangement and/or protein

structures, which could interfere with the cell behaviour within the tissue with respect to the non-irradiated cells. Therefore, in future works, the proposed approach will be extended to investigate how the mechanics and biochemical features of nuclei and whole cells change after the recovery process, and how they can be related to altered cell behaviour such as organization and growth.

Acknowledgements

We acknowledge Elettra Sincrotrone Trieste for providing access to its synchrotron radiation facilities and for financial support (Proposal numbers: 20195090, 20200312) and Dr. Silvia Bongiorno for help recording epifluorescence images.

References

- [1] Goodhead, D. T. 1989. The initial physical damage produced by ionizing radiations. *Int. J. Radiat. Biol.* 56:623-634.
- [2] Baskar, R., J. Dai, N. Wenlong, R. Yeo, and K.-W. Yeoh. 2014. Biological response of cancer cells to radiation treatment. *Frontiers Mol. Biosci.* 1:article 24.
- [3] Jeggo, P., and M.F. Lavin. 2009. Cellular radiosensitivity: how much better do we understand it? *Int. J. Radiat. Biol.*, 85(12):1061-1081.
- [4] McMahon, S.J., J. Schuemann, H. Paganetti, and K.M. Prise. 2016. Mechanistic Modelling of DNA Repair and Cellular Survival Following Radiation-Induced DNA Damage. *Sci. Rep.* 6:33290.
- [5] Borrego-Soto, G., R. Ortiz-López, and A. Rojas-Martínez. 2015. Ionizing radiation-induced DNA injury and damage detection in patients with breast cancer. *Genet. Mol. Biol.* 38(4):420-32. doi: 10.1590/S1415-475738420150019.
- [6] Lammerding, J. 2011. Mechanics of the Nucleus. *Compar. Physiol.* 1(2):783–807.
- [7] Lomakin, A.J., C.J. Cattin, D. Cuvelier, Z. Alraies, M. Molina, G.P.F. Nader, N. Srivastava, P.-J. Saez, J.M. Garcia-Arcos, I.Y. Zhitnyak, A. Bhargava, M.K. Driscoll, E.S. Welf, R. Fiolka,

- R.J. Petrie, N.S. De Silva, J.M. González-Granado, N. Manel, A.M. Lennon-Duménil, D.J. Müller, and M. Piel. 2020. The nucleus acts as a ruler tailoring cell responses to spatial constraints. *Science* 370(6514):eaba2894. doi: 10.1126/science.aba2894.
- [8] Andolfi, L, E. Bourkoula, E. Migliorini, A. Palma, A. Pucer, M. Skrap, G. Scoles, A.P. Beltrami, D. Cesselli, and M. Lazzarino. 2014. Investigation of adhesion and mechanical properties of human glioma cells by single cell force spectroscopy and atomic force microscopy, *PloS One* 9: e112582.
- [9] Grady, M.E., R.J. Composto, and D.M. Eckmann. 2016. Cell elasticity with altered cytoskeletal architectures across multiple cell types. *J. Mech. Behav. Biomed. Mater.* 61:197–207.
- [10] Deng, X., F. Xiong, X. Li, Z. Li, X. Wu, C. Guo, X. Li, Y. Li, G. Li, W. Xiong, and Z. Zeng. Application of atomic force microscopy in cancer research. 2018. *J. Nanobiotechnol.* 16,102. doi: 10.1186/s12951-018-0428-0.
- [11] Sarna, M., A. Zadlo, B. Czuba-Pelech, and K. Urbanska. Nanomechanical Phenotype of Melanoma Cells Depends Solely on the Amount of Endogenous Pigment in the Cells. 2018. *Int. J. Mol. Sci.* 19(2):607. doi: 10.3390/ijms19020607.
- [12] Jasińska-Konior, K., O. Wiecheć, M. Sarna, A. Panek, J. Swakoń, M. Michalik, K. Urbańska, and M. Elas. 2019. Increased elasticity of melanoma cells after low-Let proton beam due to actin cytoskeleton rearrangements. *Sci. Rep.* 9:7008. doi: 10.1038/s41598-019-43453.
- [13] Walpurgis, K., M. Kohler, A. Thomas, F. Wenzel, H. Geyer, W. Schänzer, and M. Thevis. 2013. Effects of gamma irradiation and 15 days of subsequent ex vivo storage on the cytosolic red blood cell proteome analyzed by 2D-DIGE and Orbitrap MS. *Proteomics Clin. Appl.* 7:561–570. doi: 10.1002/prca. 201300009.
- [14] Al Zahrani, K., and H. A. Al-Sewaidan. 2017. Nanostructural changes in the cell membrane of gamma-irradiated red blood cells. *Indian J. Hematol. Blood Transfus.* 33:109–115. doi: 10.1007/s12288-016-0657-z.

- [15] Taqi, A.H., K. Faraj, S. Zaynal, J. Said, and A. Hameed. 2019. Effects of high doses of X-Ray on hematological parameters and morphology of red blood cells in human blood. *Iran J. Med. Phys.* 16:112–119. doi: 10.22038/ijmp.2018.31184.1366.
- [16] Krause, M., J. te Riet, and K. Wolf. 2013. Probing the compressibility of tumor cell nuclei by combined atomic force–confocal microscopy. *Phys Biol.* 10:065002 (13pp). doi:10.1088/1478-3975/10/6/065002.
- [17] Pradhan, S., R. Solomon, A. Gangotra, and G.E. Yakubo. 2021. Depletion of HP1a alters the mechanical properties of MCF7 nuclei. *Biophys. J.* 120:2631–2643.
- [18] Herráez-Aguilar, D., E. Madrazo, H. López-Menéndez, M. Ramírez, F. Monroy, and J. Redondo-Muñoz. 2020. Multiple particles tracking analysis in isolated nuclei reveals the mechanical phenotype of leukemia cells. *Sci. Rep.* 10:6707.
- [19] Lipiec, E., G. Birarda, J. Kowalska, J. Lekki, L. Vaccari, A. Wiecheć, B.R. Wood, W.M. Kwiatek. 2013. A new approach to studying the effects of ionizing radiation on single cells using FTIR synchrotron microspectroscopy. *Radiat. Phys. Chem.* 93:135–141.
- [20] Meade, A.D., O. Howe, V. Unterreiner, G.D. Sockalingum, H.J. Byrne, and F.M. Lyng. 2016. Vibrational spectroscopy in sensing radiobiological effects: analyses of targeted and non-targeted effects in human keratinocytes. *Faraday Discuss.* 187:213-234.
- [21] Demir, P., and F. Severcan. 2016. Monitoring radiation induced alterations in biological systems, from molecules to tissues, through infrared spectroscopy. *Appl. Spectrosc. Rev.* 51(10):839-863.
- [22] Delfino, I., G. Perna, V. Ricciardi, M. Lasalvia, L. Manti, V. Capozzi, and M. Lepore. 2019. X-ray irradiation effects on nuclear and membrane regions of single SH-SY5Y human neuroblastoma cells investigated by Raman micro-spectroscopy. *J. Pharm. Biomed. Anal.* 164:557–573.

- [23] Delfino, I., V. Ricciardi, L. Manti, M. Lasalvia, and M. Lepore. 2019. Multivariate Analysis of Difference Raman Spectra of the Irradiated Nucleus and Cytoplasm Region of SH-SY5Y Human Neuroblastoma Cells. *Sensors* 19:3971. doi:10.3390/s19183971.
- [24] Ricciardi, V., M. Portaccio, L. Manti, and M. Lepore. 2020. An FT-IR microspectroscopy ratiometric approach for monitoring X-ray irradiation effects on SH-SY5Y human neuroblastoma cells. *Appl. Sci.* 10:2974; doi: 10.3390/app10082974.
- [25] Delfino, I., V. Ricciardi, and M. Lepore. 2022. Synchrotron FTIR microspectroscopy investigations on biochemical changes occurring in human cells exposed to proton beams. *Appl. Sci.* 12(1):336.
- [26] Gault, N., and J.L. Lefaix. 2003. Infrared microspectroscopic characteristics of radiation-induced apoptosis in human lymphocytes. *Radiat. Res.* 160:238–250.
- [27] Gasparri, F., and M. Muzio. 2003. Monitoring of apoptosis of HL60 cells by Fourier-transform infrared spectroscopy. *Biochem. J.* 369:239–248.
- [28] Meade, A., C. Clarke, H. Byrne, and F. Lyng. 2010. Fourier transform infrared microspectroscopy and multivariate methods for radiobiological dosimetry. *Radiat. Res.* 173:225–237.
- [29] Gianoncelli, A., L. Vaccari, G. Kourousias, D. Cassese, D.E. Bedolla, S. Kenig, P. Storici, M. Lazzarino, and M. Kiskinova. 2015. Soft X-ray microscopy radiation damage on fixed cells investigated with synchrotron radiation FT-IR microscopy. *Sci. Rep.* 5:10250.
- [30] Surowka, A.D., A. Gianoncelli, G. Birarda, S. Sala, N. Cefarin, A. Matruglio, M. Szczerbowska-Boruchowska, A. Ziomber-Lisiak, and L. Vaccari. 2020. Soft X-ray induced radiation damage in thin freeze-dried brain samples studied by FTIR microscopy. *J. Synchrotron Rad.* 27(5): 1218-1226.
- [31] Lipiec, E., B.R. Wood, A. Kulik, W.M. Kwiatek, and G. Dietler. 2018. Nanoscale Investigation into the Cellular response of Glioblastoma Cells Exposed to Protons. *Anal. Chem.* 90:7644–7650. doi: 10.1021/acs.analchem.8b01497.

- [32] Lipiec, E., K.R. Bambery, P. Heraud, W.M. Kwiatek, D. McNaughton, M.J. Tobin, C. Vogelb, and B.R. Wood. 2014. Monitoring UVR induced damage in single cells and isolated nuclei using SR-FTIR microspectroscopy and 3D confocal Raman imaging. *Analyst* 139:4200-4209.
- [33] te Riet, J., A.J. Katanc, C. Rankl, S.W. Stahl, A.M. Van Buul, I.Y. Phang, A. Gomez-Casado, P. Schöng, J.W. Gerritsen, A. Cambi, A.E. Rowan, G.J. Vancso, P. Jonkheijm, J. Huskens, T.H. Oosterkamp, H. Gaub, P. Hinterdorfer, G.C. Figdor, and S. Speller. 2011. Interlaboratory round robin on cantilever calibration for AFM force spectroscopy *Ultramicroscopy* 111:1659–1669.
- [34] Sneddon, I.N. 1965. The relation between load and penetration in the axymmetric Boussinesq problem for a punch of arbitrary profile. *J. Engin. Sci.* 3:47-57.
- [35] Szymanski, J.M., K. Zhang, and A.W. Feinberg. 2017. Measuring the Poisson's Ratio of Fibronectin Using Engineered Nanofibers. *Sci. Rep.* 7:13413. doi: 10.1038/s41598-017-13866-3.
- [36] Vaccari, L., G. Birarda, L. Businaro, S. Pacor, and G. Greci. 2012. Infrared, Microspectroscopy of Live Cells in Microfluidic Devices (MD-IRMS): Toward a Powerful Label-Free Cell-Based Assay. *Anal. Chem.* 84(11):4768–4775.
- [37] Baker, M.J., J. Trevisan, P. Bassan, R. Bhargava, H.J. Butler, K.M. Dorling, P.R. Fielden, S.W. Fogarty, N.J. Fullwood, K.A. Heys, C. Hughes, P. Lasch, P.L. Martin-Hirsch, B. Obinaju, G.D. Sockalingum, J. Sulé-Suso, R.J. Strong, M.J. Walsh, B.R. Wood, P. Gardner, and F.L. Martin. 2014. Using Fourier transform IR spectroscopy to analyze biological materials. *Nat. Protoc.* 9(8):1771-1791. doi: 10.1038/nprot.2014.110.
- [38] Gautam, R., B. Chandrasekar, M. Deobagkar-Lele, S. Rakshit, S. Umapathy, and D. Nandi. 2012. Identification of early biomarkers during acetaminophen-induced hepatotoxicity by Fourier transform infrared microspectroscopy. *PLoS One* 7:e45521.
- [39] Kumar, S., T. Verma, R. Mukherjee, F. Ariese, K. Somasundaram, S. Umapathy. 2016. Raman and infrared microspectroscopy: Towards quantitative evaluation for clinical research by ratiometric analysis. *Chem. Soc. Rev.* 45:1879–1900.

- [40] For details about the software, please see <https://quasar.codes/publications/>: Toplak M, et al. 2017. Infrared Orange: Connecting Hyperspectral Data with Machine Learning. *Synchrotron Rad. News* 30:40–45; Toplak M, et al. 2021. Quasar: Easy Machine Learning for Biospectroscopy. *Cells* 10:2300.
- [41] Newberg, J., J. Schimpf, K. Woods, S. Loiate, P.H. Davis, and G. Uzer. 2020. Isolated Nuclei Stiffen in Response to Low Intensity Vibration. *J. Biomech.* 111:110012. doi: 10.1016/j.jbiomech.2020.110012.
- [42] Dos Santos, A., A. Cook, R.E. Gough, M. Schilling, N.A. Olszok, I. Brown, L. Wang, J. Aaron, M.L. Martin-Fernandez, F. Rehfeldt, and C.P. Toseland. 2021. DNA damage alters nuclear mechanics through chromatin reorganization. *Nucleic Acids Research* 49:340–353.
- [43] Kim, S.-O., J. Kim, T. Okajima, N.-J. Cho. 2017. Mechanical properties of paraformaldehyde-treated individual cells investigated by atomic force microscopy and scanning ion conductance microscopy. *Nano Convergence* 4:5.
- [44] Senigagliaesi, B., G. Samperi, N. Cefarin, L. Gneo, S. Petrosino, M. Apollonio, F. Caponnetto, R. Sgarra, L. Collavin, D. Cesselli, L. Casalis, P. Parisse, 2022. Triple negative breast cancer-derived small extracellular vesicles as modulator of biomechanics in target cells. *Nanomed.: Nanotechnol. Biol. Med.* 44: 102582. <https://doi.org/10.1016/j.nano.2022.102582>.
- [45] Rowat, A.C., J. Lammerding, H. Herrmann, and U. Aebi. 2008. Towards an integrated understanding of the structure and mechanics of the cell nucleus. *Bioassays* 30:226–236.
- [46] Broers, J.L.V., E.A.G. Peeters, H.J.H. Kuijpers, J. Endert, C.V.C. Bouten, C.W.J. Oomens, F.P.T. Baaijens, and F.C.S. Ramaekers. 2004. Decreased mechanical stiffness in LMNA2/2 cells is caused by defective nucleo-cytoskeletal integrity: implications for the development of laminopathies. *Human Mol. Gen.* 13:2567–2580
- [47] Schäpe, J., S. Prauße, and M. Radmacher. 2009. Influence of Lamin A on the Mechanical Properties of Amphibian Oocyte Nuclei Measured by Atomic Force Microscopy. *Biophys. J.* 96:4319–4325.

- [48] M. Krause, F.M. Yang, M. te Lindert, P. Isermann, J. Schepensl, R.J.A. Maas, C. Venkataraman, J. Lammerding, A. Madzvamuse, W. Hendriks, J. te Riet, and K. Wolf. 2019. Cell migration through three-dimensional confining pores: speed accelerations by deformation and recoil of the nucleus. *Phil. Trans. R. Soc. B* 374:20180225.
- [49] Mazumder, A., T. Roopa, A. Basu, L. Mahadevan, and G.V. Shivashankar. 2008. Dynamics of Chromatin Decondensation Reveals the Structural Integrity of a Mechanically Prestressed Nucleus. *Biophys. J.* 95(6):P3028-3035.
- [50] Chalut, K.J., M. Höpfler, F. Lautenschläger, L. Boyde, C.J. Chan, A. Ekpenyong, A. Martinez-Arias, and J. Guck. 2012. Chromatin Decondensation and Nuclear Softening Accompany Nanog Downregulation in Embryonic Stem Cells. *Biophys. J.* 103:2060-2070.
- [51] Banyay, M., M. Sarkar, and A. Graslund. 2003. A library of IR bands of nucleic acids in solution. *Biophysical Chemistry* 104:477–488.
- [52] Gault, N., O. Rigaud, J.L. Poncy, J.L. Lefaix. 2005. Infrared microspectroscopy study of gamma-irradiated and H₂O₂-treated human cells. *Int. J. Radiat. Biol.* 81:767–779.
- [53] Barth, A. Infrared spectroscopy of proteins. 2007. *Biochim Biophys Acta – Bioenerg.* 1767(9):1073–1101. doi: 10.1016/j.bbabi.2007.06.004.
- [54] Movasaghi, Z., S. Rehman, and I. ur Rehman. 2008. Fourier Transform Infrared (FTIR) Spectroscopy of Biological Tissues. *Appl. Spectrosc. Rev.* 43(2):134-179. doi: 10.1080/05704920701829043.
- [55] Ricciardi, V., M. Portaccio, S. Piccolella, L. Manti, S. Pacifico, and M. Lepore. Study of SH-SY5Y cancer cell response to treatment with polyphenol extracts using FT-IR spectroscopy. *Biosensors* 7:57; doi: 10.3390/bios7040057.
- [56] Sofinska, K., N. Wilkosz, M. Szymonski, and E. Lipiec. 2020. Molecular Spectroscopic Markers of DNA Damage. *Molecules* 25:561; doi:10.3390/molecules25030561.
- [57] Wood, B.R. 2016. The importance of hydration and DNA conformation in interpreting infrared spectra of cells and tissues. *Chem. Soc. Rev.* 45:1980-1998.

- [58] Pelton, J.T., and L.R. McLean. 2000. Spectroscopic Methods for Analysis of Protein Secondary Structure. *Anal. Biochem.* 277:167–176.
- [59] Mei, Y., L. Miller, W. Gao, and R.A. Gross. 2003. Imaging the distribution and secondary structure of immobilized enzymes using infrared microspectroscopy. *Biomacromolecules* 4:70–74.
- [60] Delfino, I., M. Portaccio, B. Della Ventura, D.G. Mita, and M. Lepore. 2013. Enzyme distribution and secondary structure of sol-gel immobilized glucose oxidase by micro-attenuated total reflection FT-IR spectroscopy. *Mater. Sci. Eng. C* 33:304–310.
- [61] Evich, M., A.M. Spring-Connell, and M.W. Germann. 2017. Impact of modified ribose sugars on nucleic acid conformation and function. *Heterocycl. Commun.* 23(3):155–165.
- [62] Dovbeshko, G. 2000. FTIR spectroscopy studies of nucleic acid damage. *Talanta* 53:1. doi: 10.1016/S0039-9140(00)00462-8.
- [63] Weijers, R.M.N. 2016. Membrane flexibility, free fatty acids, and the onset of vascular and neurological lesions in type 2 diabetes. *J. Diab. Metabol. Disord.* 15:13. DOI 10.1186/s40200-016-0235-9.
- [64] Bennetzen, M.V., D.H. Larsen, J. Bunkenborg, J. Bartek, J. Lukas, and J.A. Andersen. 2010. Site-specific Phosphorylation Dynamics of the Nuclear Proteome during the DNA Damage Response. *Mol. Cell Proteomics* 9(6):1314–1323. doi: 10.1074/mcp.M900616-MCP200.
- [65] Anderson, L., C. Henderson, and Y. Adachi. 2001. Phosphorylation and rapid relocalization of 53BP1 to nuclear foci upon DNA damage. *Mol. Cell Biol.* 21(5):1719-1729. doi: 10.1128/MCB.21.5.1719-1729.2001.
- [66] Izumi, Y., K. Fujii, F. Wien, C. Houée-Lévin, S. Lacombe, D. Salado-Leza, E. Porcel, R. Masoud, S. Yamamoto, M. Réfrégiers, M.-A. Hervé du Penhoat, and A. Yokoya. 2016. Structure Change from b-Strand and Turn to a-Helix in Histone H2A-H2B Induced by DNA Damage Response. *Biophys. J.* 111:69–78, 2016. doi: 10.1016/j.bpj.2016.06.002.

- [67] Izumi, Y., K. Fujii, S. Yamamoto, K. Matsuo, H. Namatame, M. Taniguchi, and A. Yokoya. 2017. DNA damage response induces structural alterations in histone H3–H4. *J. Radiat. Res.* 58(1):59–65. doi: 10.1093/jrr/rrw086.
- [68] Oldenhof, H., S. Schutze, W.F. Wolkers, and H. Sieme. 2016. Fourier transform infrared spectroscopic analysis of sperm chromatin structure and DNA stability. *Andrology* 4:430–441.
- [69] Hermine, T., N.J. Jones, J.M. Parry. 1997. Comparative induction of micronuclei in repair-deficient and -proficient Chinese hamster cell lines following clastogen or aneugen exposures. *Mutat. Res.* 392:151–163. doi: 10.1016/s0165-1218(97)00053-0.
- [70] Marcon, F., R. Meschini, E. Iorio, S. Palleschi, G. De Luca, E. Siniscalchi, L. Conti, M. Chirico, M.E. Pisanu, F. De Battistis, B. Rossi, A. Minoprio, A. Giuliani, P. Karran, M. Bignami. 2022. Young transgenic hMTH1 mice are protected against dietary fat-induced metabolic stress—implications for enhanced longevity. *Aging Cell* 00:e1360. doi: 10.1111/accel.13605.